

# Ultrafine Iron Boride as a Highly Efficient Nanocatalyst Expedites Sulfur Redox Electrochemistry for High-Performance Lithium-Sulfur Batteries

Guxian Chen,<sup>[a]</sup> Hongyang Li,<sup>[a]</sup> Yuqi Wang,<sup>[a]</sup> Yingrui Ding,<sup>[a]</sup> Pengsen Qian,<sup>[a]</sup> Kailong Zhang,<sup>\*[b]</sup> Haibo Zeng,<sup>\*[a]</sup> and Gaoran Li<sup>\*[a]</sup>

Lithium-sulfur (Li–S) batteries have garnered significant interest as a strong contender for future energy storage, characterized by their remarkable energy density and cost-effectiveness. However, the sluggish conversion kinetics of the polysulfide intermediates, compounded with their shuttling behaviors, pose considerable challenges in sulfur electrochemistry. Herein, we develop a novel iron monoboride (FeB) electrocatalyst for boosting sulfur reactions and enhancing Li–S battery performance. The ultrafine powdery FeB affords abundant and fully exposed active interfaces for host-guest interactions. Meanwhile, the intrinsic high conductivity of FeB, combined with its strong adsorption and catalytic activity to polysulfides, enables

substantial inhibition of the shuttle effect and enhancement of conversion kinetics. As a result, sulfur electrodes equipped with the FeB nanocatalyst realize excellent cyclability with a minimal capacity fading of 0.04% per cycle over 500 cycles, as well as favorable rate capability up to 7 C. Moreover, decent areal capacity and cycling stability can be also achieved under high-loading ( $5.1 \text{ mg cm}^{-2}$ ) and limited-electrolyte ( $7.0 \text{ mL g}^{-1}$ ) configurations. This study presents a facile approach and insightful perspective on nanostructured metal boride for highly efficient sulfur electrocatalysis, holding good promise for the advancement of high-performance Li–S batteries.

## Introduction

Lithium-sulfur (Li–S) batteries are among the most promising candidates for next-generation energy storage, attributed to their favorable attributes including the high energy density of  $2600 \text{ Wh kg}^{-1}$ , almost five times that of conventional lithium-ion batteries, alongside the cost-effectiveness and environmental benignity.<sup>[1–3]</sup> Despite these advantages, several formidable challenges afflict battery electrochemistry and impede the realization of practically viable performance. Specifically, the low electrical and ionic conductivities of sulfur and its lithiation product,  $\text{Li}_2\text{S}$ , dictate sluggish reaction kinetics and low utilization of active material. Moreover, the presence of solid-liquid phase transformation further exacerbates the redox kinetics by necessitating additional energy to overcome nucleation/denucleation barriers. Meanwhile, the so-called “shuttle effect”, triggered by the high solubility and mobility of the intermediate lithium polysulfides (LiPSs), engenders continuous sulfur loss, coulombic inefficiency, and electrode passivation during cycling.<sup>[4–6]</sup> These issues, combined with the intrinsic

irreversibility of lithium electrochemistry, lead to the low capacity and fast degradation of Li–S batteries.<sup>[7,8]</sup>

In response to these challenges, extensive research endeavors have been directed towards the development of functional materials to promote and stabilize sulfur electrochemistry.<sup>[9,10]</sup> Nanostructured carbon materials dominate the initial investigations owing to their high conductivity, lightweight nature, and favorable structural adaptability to accommodate active sulfur species. Various carbon structures, such as mesoporous carbon, hollow carbon, spheres, graphene, etc.<sup>[11–13]</sup> have been meticulously engineered to serve as host materials for sulfur electrodes, yielding noteworthy enhancements in battery performance. Nevertheless, nonpolar carbon materials exhibit limited capability in adsorbing LiPSs, thus lacking chemical constraints against their shuttling behaviors. Consequently, polar materials, typified by metal oxides and sulfides, garnered significant attention during the past few years due to their good LiPS adsorption and catalytic activities.<sup>[14–16]</sup> Despite the many endeavors and notable strides, two principal challenges persist in these materials, namely, low intrinsic conductivity and limited active sites, posing barriers to the further advancement of Li–S battery performance.

Recently, metal borides (MBs) have emerged as a novel and promising family of sulfur electrocatalysts aiming at tackling the abovementioned challenges.<sup>[17–19]</sup> MBs generally comprise boron and metal elements bonded via covalent interactions. The strong hybridization between metal d orbitals and boron p orbitals near the Fermi level confers metallic conductivity that surpasses that of many conventional metal compounds.<sup>[20,21]</sup> Apart from that, the localized ionic M–B bonding imparts certain chemical polarity to MBs, fostering favorable adsorption

[a] G. Chen, H. Li, Y. Wang, Y. Ding, P. Qian, H. Zeng, G. Li  
School of Materials Science and Engineering, Nanjing University of Science and Technology, Nanjing 210094, China  
E-mail: zeng.haibo@njjust.edu.cn  
gaoranli@njjust.edu.cn

[b] K. Zhang  
National & Local Joint Engineering Research Center for Mineral Salt Deep Utilization, Huaiyin Institute of Technology, Huai'an 223003, China  
E-mail: klzhang@hyit.edu.cn

 Supporting information for this article is available on the WWW under <https://doi.org/10.1002/batt.202400128>

and catalysis of LiPSs. Leveraging these unique advantages, MBs received significant research enthusiasm in Li–S batteries and have demonstrated notable progress. Pioneering research by Qian's group introduced conductive and layer-structured TiB<sub>2</sub> as a sulfur host material,<sup>[22]</sup> proposing a surface vulcanization mechanism to effectively confine LiPSs for alleviating the shuttle effect and enhancing battery cyclability. NbB<sub>2</sub> was revealed to regulate the 3D nucleation and growth of Li<sub>2</sub>S, which decreases the reaction barrier and promotes fast LiPS conversions.<sup>[23]</sup> Very recently, our group developed the unique CrB with dual sulfophilicity for sulfur electrocatalysis.<sup>[24]</sup> The coexistence of Cr–S and B–S bonding strongly confines LiPSs and catalyzes their conversions, resulting in significantly improved cycling stability and rate capability even under high sulfur loading and lean electrolyte. These advances collectively underscore the immense potential of MBs in catalyzing sulfur reactions and enhancing battery performance. However, research and development of MBs as sulfur electrocatalysts are still in their infancy. The MB catalyst family requires considerable expansion to establish the related system, while the underlying catalytic mechanism awaits further and in-depth investigations.

Compared with other metals, iron boasts abundant reserves and is environmentally friendly.<sup>[25,26]</sup> Thus, iron borides are expected to serve as cost-effective and highly active sulfur electrocatalysts, yet the related studies remain sparse. In this contribution, we developed for the first time the ultrafine iron monoboride (FeB) as an advanced sulfur electrocatalyst. The FeB nano-powder was prepared via a molten-salt method. In contrast to conventional synthesis approaches, the localized reaction mediated by molten salt ensures well-controlled particle size and uniformity under high temperature and ambient pressure. The obtained FeB nanoparticles deliver ultrafine dispersity, with an average size of around 13 nm, thus fully exposing active surfaces for high-efficiency sulfur electrocatalysis. Moreover, strong chemical adsorption between FeB and LiPSs can be established, leading to significantly reduced reaction barriers and accelerated conversion kinetics. As a result, sulfur electrodes based on FeB realize a minimal capacity fading rate of only 0.04% per cycle over 500 cycles at 1 C, as well as a good rate capability that retains 533.8 mAh g<sup>-1</sup> at a high rate of 7 C. Besides, decent areal capacity (5.75 mAh cm<sup>-2</sup>) and cyclability are also achievable under high sulfur loading and limited electrolyte, highlighting the good potential for the development of high-performance and practically viable Li–S batteries.

## Results and Discussion

The FeB nanocatalyst was prepared via a one-pot molten-salt method, wherein FeSO<sub>4</sub> served as the iron source and NaBH<sub>4</sub> acted as both the boron source and reductive agent. Typically, the reaction between FeSO<sub>4</sub> and NaBH<sub>4</sub> powders is highly exothermic and prone to spontaneous ignition, leading to a self-propagating high-temperature synthesis (SHS).<sup>[27,28]</sup> However, the rapid and vigorous SHS process is hard to control and

often results in the formation of non-equilibrium phases and incomplete reactions. In our approach, a molten-salt media (consisting of KCl and NaCl) is introduced to regulate the reaction rate. The presence of surrounding molten salts serves to temper the SHS reaction and mitigate the particle overgrowth. It is also worth noting that the molten-salt method offers simplicity in setup and operates under relatively mild conditions, demonstrating favorable scalability.

Figure 1a shows the X-ray diffraction (XRD) pattern of the as-prepared FeB. A group of sharp peaks at 32.5, 37.7, 45.0, 47.7, 57.6, and 63.0 degrees can be observed, corresponding to the (020), (101), (021), (210), (211), and (002) facets, respectively, of orthorhombic FeB in the Pbmm space group (PDF#32-0463).<sup>[29,30]</sup> No other species can be detected, indicating the successful preparation of FeB in good crystallinity and purity. Figure 1b illustrates the crystallographic structure of FeB, wherein boron atoms form zig-zag chains, and parallel chains collectively constitute the boron layer. Interposed within these layers are the iron atomic layers, contributing to a 2D interstitial alloying structure that underpins the excellent conductivity of FeB.<sup>[31]</sup> The electrical conductivity of the obtained FeB was measured to be 325.6 Sm<sup>-1</sup>, comparable to that of super P (SP, 419.2 Sm<sup>-1</sup>), and much higher than FeS<sub>2</sub> (192.3 Sm<sup>-1</sup>) and Fe<sub>2</sub>O<sub>3</sub> (10<sup>-4</sup> Sm<sup>-1</sup>).<sup>[32,33]</sup> This notable conductivity is expected to provide a fast electron supply for accelerating the electrochemical conversions of active sulfur.

The surface chemistry of FeB was investigated using X-ray photoelectron spectroscopy (XPS). The survey spectrum verifies the existence of Fe and B in the product (Fig. S1). The high Fe 2p spectrum exhibits two peaks at 707.3 and 711.0 eV, attributed to the Fe–B bond with a Fe(0) valence and the Fe–O bond with a higher Fe valance, respectively (Figure 1c).<sup>[34,35]</sup> This observation suggests the formation of metallic FeB alongside partial surface oxidization. Accordingly, peaks corresponding to B–Fe and B–O are detected at 188.1 and 191.9 eV, respectively, in the B 1s spectrum (Figure 1d).<sup>[36,37]</sup> These findings align with the literature, further confirming the successful preparation of FeB. The metallic nature of FeB is expected to facilitate rapid charge transfer for sulfur reactions, while the localized Fe–B polarity engenders potential chemical interactions with LiPSs for inhibiting the shuttle effect and promoting reaction kinetics.

The morphology and microstructure of the as-prepared FeB were investigated using scanning electron microscopy (SEM). Figure 2a and b illustrate the ultrafine and well-dispersed nanoparticulate structure of FeB, wherein the nanoparticles interconnect to form pathways for fast electron transfer. Transmission electron microscope (TEM) characterization was carried out for further structural analysis. The interconnected nanoparticles are more clearly observed with a grain size concentrated around 13 nm (Figure 2c and Figure S2). It is noted that even under a relatively high annealing temperature of 1000 °C, ultrafine nanometric structure can be still achieved, showcasing the great superiority of the molten-salt method in alleviating the SHS effect, constraining the local boronization reaction, and controlling the grain growth of the FeB product. In addition, distinct lattice fringes are noticed in the high-resolution TEM image (Figure 2d). The corresponding inverse fast Fourier trans-

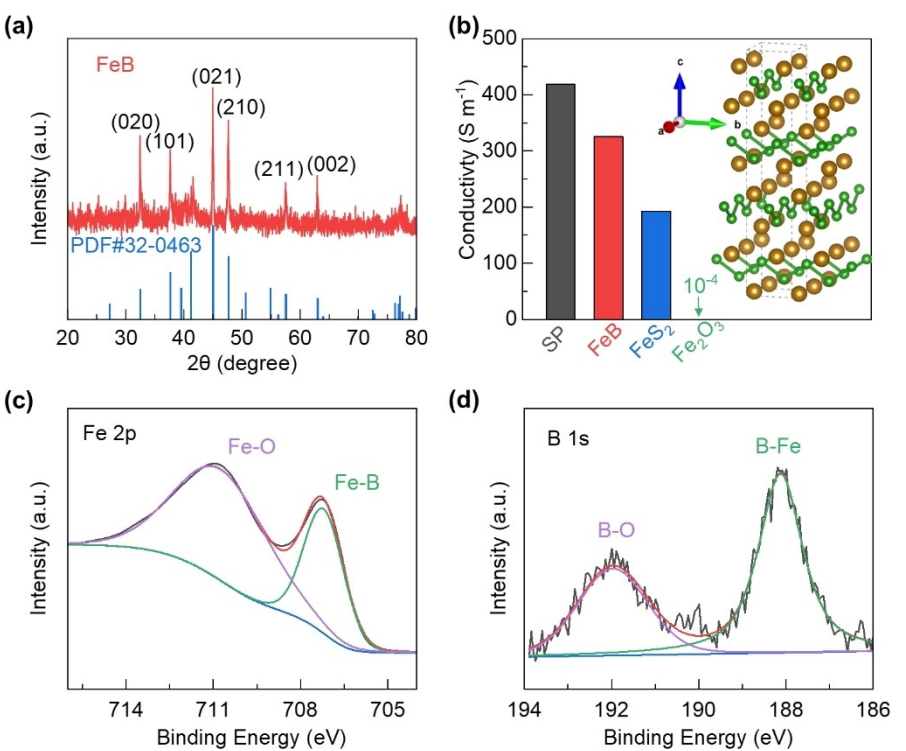


Figure 1. (a) XRD pattern, (b) crystalline structure and electrical conductivity, and high-resolution XPS (c) Fe 2p and (d) B 1s spectra of FeB.

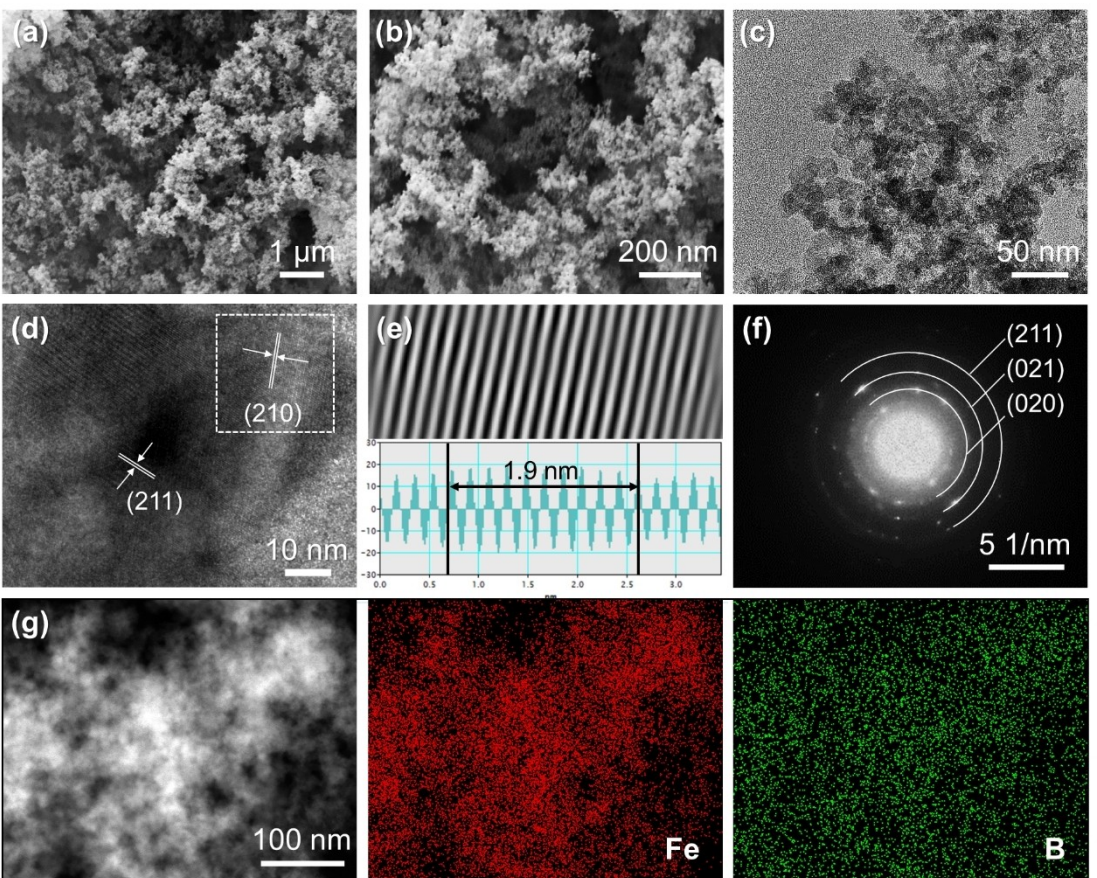
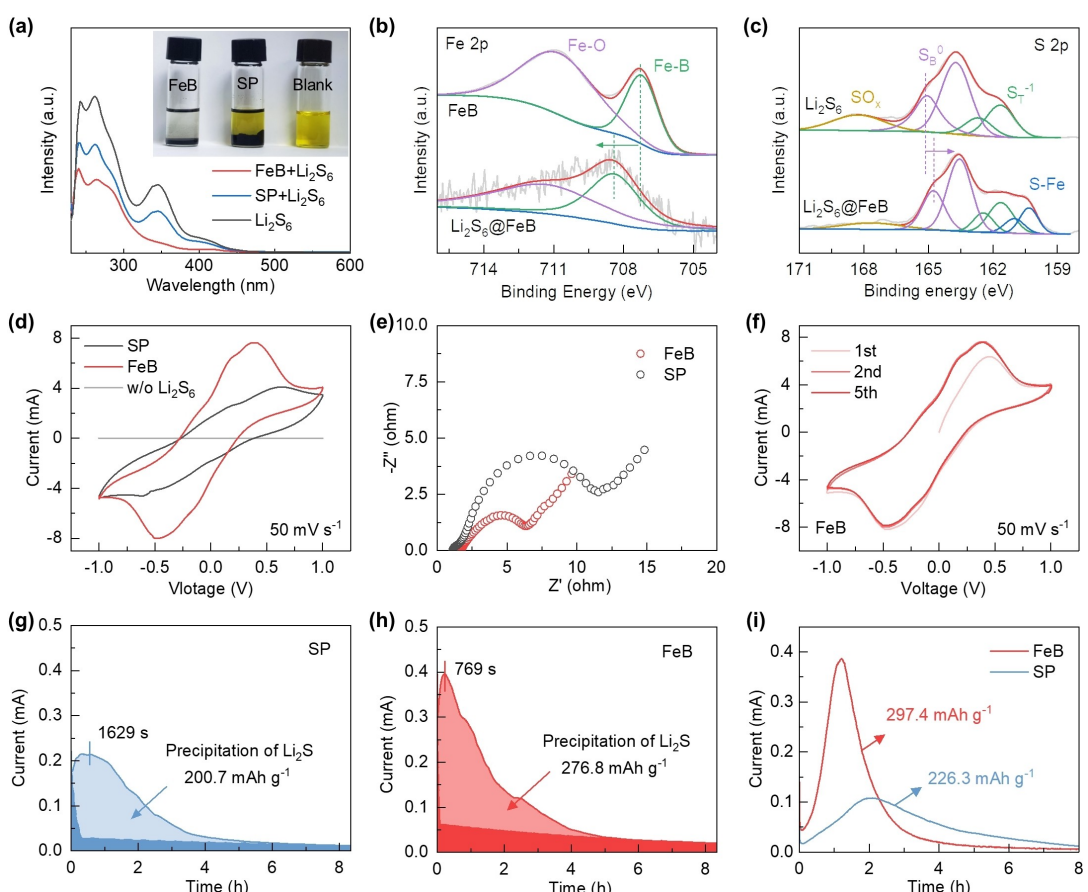


Figure 2. (a, b) SEM images, (c, d) TEM images and the corresponding IFFT and line intensity profile of the selected region, (f) SAED pattern, (g) HADDF-STEM image and elemental mapping of FeB.

form (IFFT) results reveal the interplanar spacing of 0.19 and 0.16 nm, referring to the (210) and (211) crystal facets of orthorhombic FeB, respectively (Figure 2e and Figure S3).<sup>[38]</sup> Also, the selected area electron diffraction (SAED) pattern reveals the polycrystalline character (Figure 2f), with the marked rings assigned to the (211), (021), and (020) facets of FeB.<sup>[39]</sup> Figure 2g shows the high-angle annular dark field scanning transmission electron microscopy (HADDF-STEM) image and the corresponding element mapping of FeB. Uniform distributions of Fe and B can be noted, further confirming the excellent dispersity of FeB. Based on the above results, it can be concluded that ultrafine and powdery FeB nanoparticles are successfully prepared via the molten-salt method, which is expected as a good sulfur electrocatalyst.

The chemical interaction between FeB and LiPSs holds significant importance in sulfur electrocatalysis, which was studied by static adsorption and XPS analysis. The inset of Figure 3a presents the light-yellow color of the blank Li<sub>2</sub>S<sub>6</sub> solution. After the immersion of FeB for 6 h, notable decoration of the Li<sub>2</sub>S<sub>6</sub> solution can be noticed, while the contrast sample based on the same mass of SP remains persistently yellow. Such a dramatic comparison strongly indicates the excellent LiPS adsorbability of FeB, which is verified by its notably lower UV-vis absorbance of the supernatant compared with other

samples (Figure 3a).<sup>[40]</sup> The underlying adsorption mechanism is elucidated through XPS analysis. Figure 3b illustrates that after the LiPS adsorption, the Fe–B peak shifts to a higher binding energy range, suggesting a decreased electron cloud density of Fe. This should be attributed to the electron transfer from metallic Fe to electron-deficient S upon the FeB-LiPS interaction, differing from the conventional Lewis acid-base mode in catalysts such as metal oxides or sulfides.<sup>[41,42]</sup> Accordingly, a new pair of peaks emerges at around 160 eV in the S 2p spectra after LiPS adsorption (Figure 3c), further validating the formation of the Fe–S bond.<sup>[43]</sup> The negative shift of the bridging sulfur (S<sub>B</sub><sup>0</sup>) peaks also signifies sulfur reduction due to the acceptance of electrons donated by Fe, aligning well with the proposed interaction mode.<sup>[44]</sup> Meanwhile, the B–Fe peak in the B1s spectra is significantly weakened after LiPS adsorption (Figure S4a). This peak reduction is likely attributed to two aspects: the oxidization of Fe consuming the surface B–Fe species and masking the signals from the inner part, and the oxidization of B via the formation of B–S that may contribute to the broadened band at the higher energy range.<sup>[24]</sup> The Li 1s spectra were also collected (Figure S4b), revealing the broadened and negatively shifted peak, likely due to the coordination of Li–B similar to the “lithium bond” reported previously.<sup>[45]</sup> Considering the notable shift of the Fe 2p peaks and the



**Figure 3.** (a) LiPS adsorption by different samples and the corresponding UV-vis spectra; (b) Fe 2p and (c) S 2p XPS spectra before and after LiPS adsorption on FeB; (d) CV profiles and (e) Nyquist plots of different symmetric cells; (f) CV profiles of symmetric FeB cell at different cycles; (g, h) Li<sub>2</sub>S precipitation and (i) decomposition profiles on SP and FeB electrodes.

distinct emergence of S–Fe bonding in the XPS spectra, which suggests a strong interaction between Fe and polysulfide, we posit Fe to be the primary active site. More definitive confirmation awaits subsequent investigations. Collectively, these results underscore the robust chemical interactions between FeB and LiPSs, which are expected to effectively confine the active species and promote their catalytic conversions for fast and durable sulfur electrochemistry.

Given this, symmetric cells were first assessed to study the catalytic effect. Figure 3d shows the cyclic voltammetry (CV) profiles of symmetric cells based on bare SP and FeB at a scanning rate of  $50 \text{ mVs}^{-1}$ . The cell in the absence of  $\text{Li}_2\text{S}_6$  exhibits almost undetectable redox peaks, indicating that the capacity is mainly contributed by the LiPS conversions. It is also noted that the FeB-based symmetric cell shows a much higher current response with smaller potential gaps between the redox peaks compared with the SP cell, indicating the promoted LiPS conversions by the FeB catalyst. Such an improvement can be supported by the Nyquist plots as shown in Figure 3e. Much smaller electrochemical impedance can be realized in the FeB-based configuration, fostering faster charge transfer for sulfur redox reactions. Additionally, the CV profile of the FeB cell can be well maintained over multiple cycles (Figure 3f), suggesting good electrochemical reversibility. Aside from the bidirectional conversion of soluble LiPS, the liquid-to-solid reduction with

the precipitation of  $\text{Li}_2\text{S}$  is another kinetically challenging process in sulfur electrochemistry. Therefore, the  $\text{Li}_2\text{S}$  precipitation on SP and FeB was compared to further study the catalytic behaviors. Figure 3g and h illustrate the chronoamperometric curves for potentiostatic LiPS reduction on different surfaces. The initial downslope and the level-off current (dark region) correspond to the reduction of high-order LiPS residues into low-order species, while the major upward peak (light region) is assigned to the  $\text{Li}_2\text{S}$  nucleation and precipitation.<sup>[46]</sup> Comparative analysis reveals that the FeB catalyst enables a much earlier peak position (769 vs. 1629 s), sharper peak shape, and higher precipitation capacity ( $276.8 \text{ vs. } 200.7 \text{ mA}\text{h g}^{-1}$ ) compared with its SP counterpart, indicating the lower energy barrier and higher efficiency for  $\text{Li}_2\text{S}$  precipitation on the FeB surface. Furthermore, the reverse  $\text{Li}_2\text{S}$  decomposition and oxidation behaviors were also studied by potentiostatic charging (Figure 3i). Similarly, earlier peak position and larger capacity are also achieved by the FeB electrode in comparison with the SP electrode, consistently certifying the enhanced  $\text{Li}_2\text{S}$  redox kinetics by the FeB catalyst. These results collectively validate the excellent catalytic effect of the as-developed FeB for promoting bidirectional sulfur conversions, holding a good promise for improving Li–S battery performance.

In light of these advancements, the actual catalytic effect was further evaluated in Li–S coin cells. Figure 4a depicts the

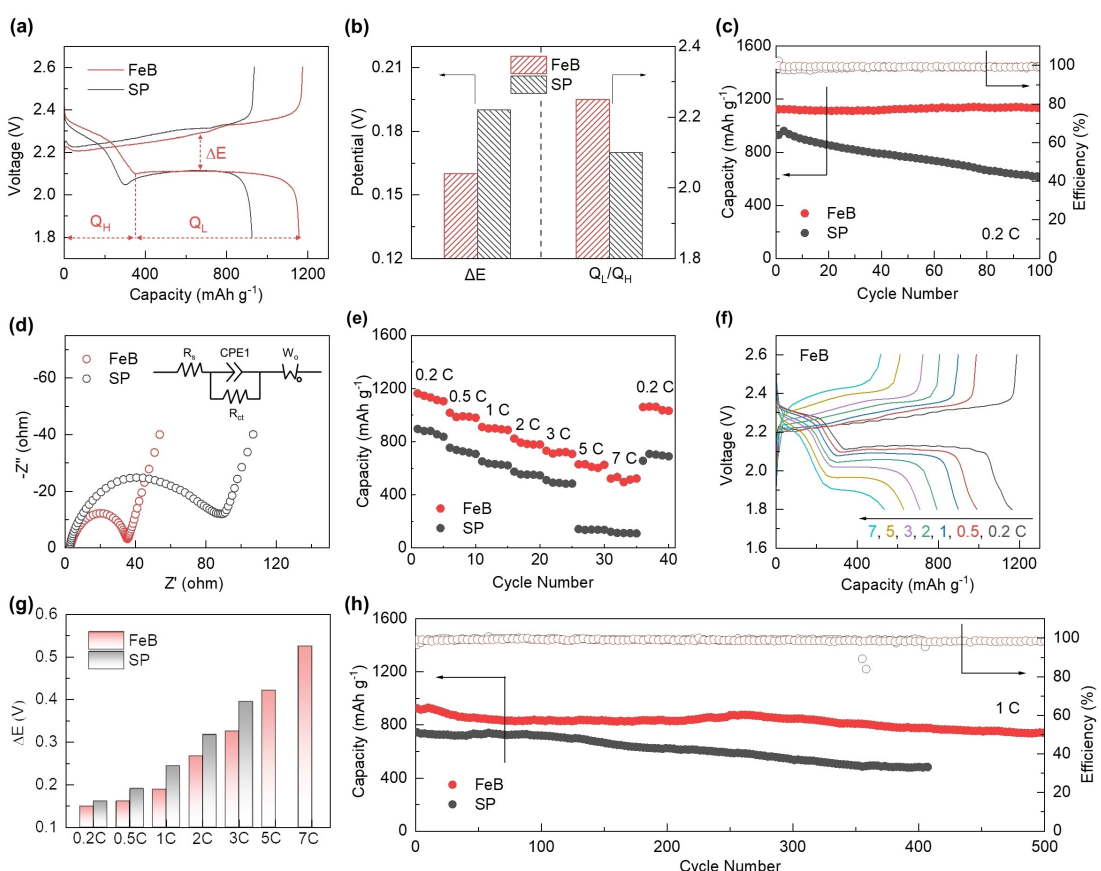


**Figure 4.** (a) Charge-discharge profiles, (b)  $\Delta E$  and  $Q_L/Q_H$  ratios, (c) cycling performance at  $0.2 \text{ C}$ , (d) Nyquist plots, and (e) rate performance of FeB and SP cells; (f) voltage profiles of FeB electrode under different current rates; (g) charge-discharge  $\Delta E$  at different rates and (h) long-term cycling performance of different electrodes.

charge-discharge curves of sulfur electrodes based on bare SP and FeB. The voltage profiles of both electrodes exhibit a two-plateau discharge curve, corresponding to the reduction from element sulfur to long-chain LiPSs ( $\text{Li}_2\text{S}_x$ ,  $4 \leq x \leq 8$ ) and further into the insoluble  $\text{Li}_2\text{S}_2/\text{Li}_2\text{S}$ . A relatively long and smooth slope can be witnessed during the charging process, referring to the inverse oxidization of  $\text{Li}_2\text{S}_2/\text{Li}_2\text{S}$  into element sulfur.<sup>[47]</sup> The FeB electrode delivers a capacity of  $1156.9 \text{ mAh g}^{-1}$ , much higher than that of the SP counterpart ( $925 \text{ mAh g}^{-1}$ ). Besides, a smaller potential gap ( $\Delta E$ ) between charge and discharge plateaus can be noted (0.16 vs. 0.19 V), suggesting a limited electrochemical polarization due to the effective sulfur electrocatalysis by FeB (Figure 4b). Meanwhile, a higher ratio of low-plateau versus high-plateau discharge capacities ( $Q_L/Q_H$ ) can be also achieved by the FeB electrode (2.25 vs. 2.10), manifesting that the LiPSs dissolved during the high-plateau discharging can be effectively reutilized and precipitated back onto the electrode during the low-plateau stage. These results consistently and collectively demonstrate the fast and efficient sulfur redox behaviors on the FeB electrode.

The galvanostatic cycling performance of different electrodes was compared in Figure 4c. The FeB electrode exhibits excellent cycling stability with a capacity retention of  $1124.1 \text{ mAh g}^{-1}$  after 100 cycles at 0.2 C. By contrast, the SP electrode undergoes much faster capacity decay, retaining only  $618.8 \text{ mAh g}^{-1}$  by the 100<sup>th</sup> cycle. Moreover, a consistently higher coulombic efficiency can be obtained for the FeB electrode compared with its SP counterpart, suggesting the effective inhibition of the shuttle effect and enhanced electrochemical reversibility in the FeB-based configuration. This electrochemical advancement is further evidenced by EIS characterization. Figure 4d shows the Nyquist plots of the SP and FeB electrodes. Both spectra consist of a semicircle at high-medium frequency and an oblique line at low frequency, which refers to the charge transfer ( $R_{ct}$ ) and Warburg resistance, respectively.<sup>[48]</sup> A much smaller  $R_{ct}$  of the FeB electrode can be noticed compared with that of the SP electrode, reflecting the facile charge transfer therein for powering the rapid sulfur reactions.<sup>[49]</sup> Apart from that, the cycling performance of sulfur electrodes equipped with different contents of FeB catalyst was studied, as depicted in Figure S5. On the one hand, a lower content of FeB (2 wt.%) also enhances the cycling stability compared with its SP counterpart, yet is inferior to that with 10 wt.% FeB due to the limited catalytic sites. On the other hand, the overdose of FeB (20 wt.%) lowers the capacity likely due to the decrease of porosity and destruction of ion/mass transfer pathways within the electrode. Thus, a content of 10 wt.% was regarded as optimal for Fe addition in the sulfur electrodes.

The rate performance was also examined by cycling at varied current rates, as presented in Figure 4e. It is noted that the FeB electrode retains a favorable capacity of  $533.8 \text{ mAh g}^{-1}$  even under a high rate of up to 7 C and is capable of recovering to  $1064.0 \text{ mAh g}^{-1}$  as the applied current returns to 0.2 C. Whereas, for the SP electrode, much faster capacity attenuation is noticed along with the increase of current, retaining only  $140.3 \text{ mAh g}^{-1}$  at 7 C. Such a distinctive comparison strongly

manifests the superior reaction kinetic realized by the FeB electrocatalyst, which lowers the energy barriers and promotes the bidirectional sulfur conversions for superior rate capability. This kinetic improvement can be more vividly demonstrated by the evolution of the voltage profile during the multi-rate cycling. Figure 4f presents the voltage profiles of the FeB electrode at different current rates. It is discernable that the potential gap between the charge and discharge plateaus gradually expands with the rate increase from 0.2 to 7 C, yet the two-platform discharge profile can be maintained for the FeB electrode. By contrast, the SP electrode experiences much more severe polarization and fails to maintain the two-plateau profile since 5 C (Figure S6). The evolution of the potential gap along with the increase of the current rate are summarized and compared in Figure 4g. Based on these advancements, a long-term cycling evaluation was carried out for the FeB electrode. As shown in Figure 4h, outstanding cycling stability can be achieved with a minimal capacity fading rate of 0.04% per cycle over 500 cycles at 1 C. By contrast, the SP electrode displays a much faster capacity attenuation of 0.07% per cycle and fails reversible cycling beyond the 407<sup>th</sup> cycle. In addition, a high coulombic efficiency close to unity is sustained for the FeB electrode throughout the cycling, indicative of excellent sulfur redox reversibility. It is also noteworthy that these achieved performances are highly competitive among recent literature based on metal borides and other conventional metal compounds (Table S1), further highlighting the superiority of the FeB electrocatalyst design.

To further understand these electrochemical advancements, the CV profiles of the FeB and SP electrodes were collected as shown in Figure 5a. Both curves exhibit two cathodic peaks at around 2.3 V and 2.0 V, and overlapped peaks at around 2.35 V during the anodic scanning, which echoes the charge-discharge profiles in line with the typical multi-step sulfur conversion electrochemistry. Notably, stronger current response and smaller potential gaps between redox peaks can be observed for the FeB electrode compared with those of the SP counterpart, manifesting enhanced conversion kinetics and reduced overpotential. Apart from that, multiple scanning rates from 0.1 to  $0.5 \text{ mV s}^{-1}$  were applied for the CV measurement (Figure 5b and Figure S7). A mitigated redox polarization upon the increase of scanning rate is observed for the FeB electrode, further evidencing the promoted sulfur reactions compared with that based on bare SP. Linear fitting between the peak current ( $I_p$ ) and the square root ( $v^{0.5}$ ) of the scanning rate at different peaks (I, II, and III as marked in Figure 5b) was carried out for different electrodes and compared in Figure 5c–e. According to the Randles-Sevcik principle, the slope of the fitted line is directly proportional to the  $\text{Li}^+$  diffusion coefficient ( $D_{\text{Li}^+}$ ), a critical factor influencing kinetic properties. As shown in Figure 5f, the FeB electrode presents a much higher slope than that of the SP electrode at all these peaks, confirming its high  $D_{\text{Li}^+}$  that facilitates the charge transfer for fast sulfur conversion reactions.<sup>[50]</sup> On this basis, the galvanostatic intermittent titration technique (GITT) profiles of different sulfur electrodes were recorded to further explore the kinetic enhancement (Figure 5g). The IR drop, which is identified as the potential gap

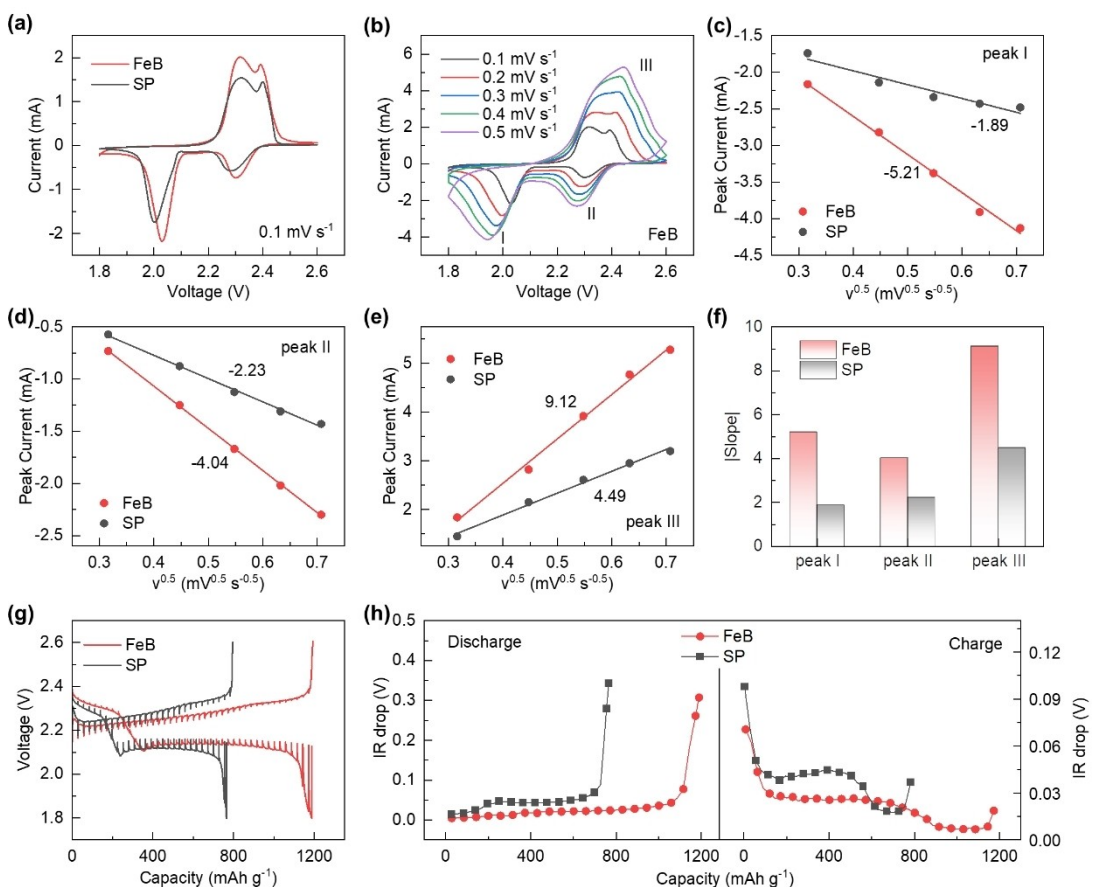


**Figure 5.** (a) CV curves of FeB and SP electrodes at  $0.1 \text{ mV s}^{-1}$ ; (b) CV curves of the FeB electrode at different scanning rates; (c-e)  $I_p-v^{0.5}$  linear fitting at peak I, II, and III in the CV profiles; (f) summary of the slopes of the fitting lines; (g) GITT profiles of different electrodes and (h) the corresponding IR drop evolution along the charge/discharge process.

between the equilibrium and dynamic (with current applied) states, was collected at a series of charge and discharge depths to study the dynamic polarization during the charge and discharge processes (Figure 5h). Throughout the cycle, the FeB electrode consistently exhibits lower IR drops, indicating smaller internal resistance reflective of the higher electrical conductivity and  $D_{\text{Li}^+}$  for facilitating sulfur reactions.

Given this, a series of EIS studies was conducted to probe into the electrochemical impedance. Figure 6a and b show the Nyquist plots of the FeB and SP cells at various temperatures. It can be noticed the internal resistance of both cells decreases with increasing temperature due to the enhanced mobility of electrons and ions. By comparison, the resistance in the FeB electrode remains consistently lower than that of the SP electrode, confirming the facile charge transfer and stable electrode/electrolyte interface. The related activation energy was calculated by linearly correlating the inverse of absolute temperature with logarithmic values of the reciprocal of charge transfer resistance based on the Arrhenius Law (Figure 6c).<sup>[51]</sup> A lower activation energy of  $44.6 \text{ kJ mol}^{-1}$  is obtained for the FeB electrode compared with its SP counterpart ( $56.9 \text{ kJ mol}^{-1}$ ), indicating that the FeB effectively lowers the energy barriers for sulfur conversions and enhances the reaction kinetics. The evolution of the Nyquist plot during the discharge process was

further recorded (Figure 6d and e). It is noted that the cell impedance increases as discharging initiates, ascribed to the generation and dissolution of LiPSs that elevate electrolyte viscosity and hinder ion transfer. As the cells are further discharged, the precipitation of  $\text{Li}_2\text{S}$  lowers the LiPS concentration in the electrolyte and thus decreases the charge transfer impedance. Nyquist plots of different cells were further fitted, with the evolution of the resulting resistances summarized and compared in Figure 6f-h. It is evident that the FeB electrode delivers much lower values for all the solution ( $R_s$ ), charge transfer ( $R_{ct}$ ), and Warburg resistance ( $R_w$ ) compared with those of the SP electrode, collectively confirming that the highly conductive and catalytic FeB effectively reduces energy barrier and facilitates charge transfer, facilitating the rapid sulfur conversions with significantly enhanced battery performance.

Given these improvements, FeB electrodes under high sulfur loading and limited electrolyte were further examined to explore their potential for practical application. Figure 7a displays the cycling behaviors of FeB electrodes under different sulfur loading at 0.1 C. High areal capacities of 3.20, 4.43, and  $5.75 \text{ mAh cm}^{-2}$  are achieved as the sulfur loading increases to 2.8, 3.7, and  $5.1 \text{ mg cm}^{-2}$ , respectively, with good cycling stabilities. The voltage profiles of the FeB electrode under a sulfur loading of  $3.7 \text{ mg cm}^{-2}$  and electrolyte-to-sulfur (E/S) ratio

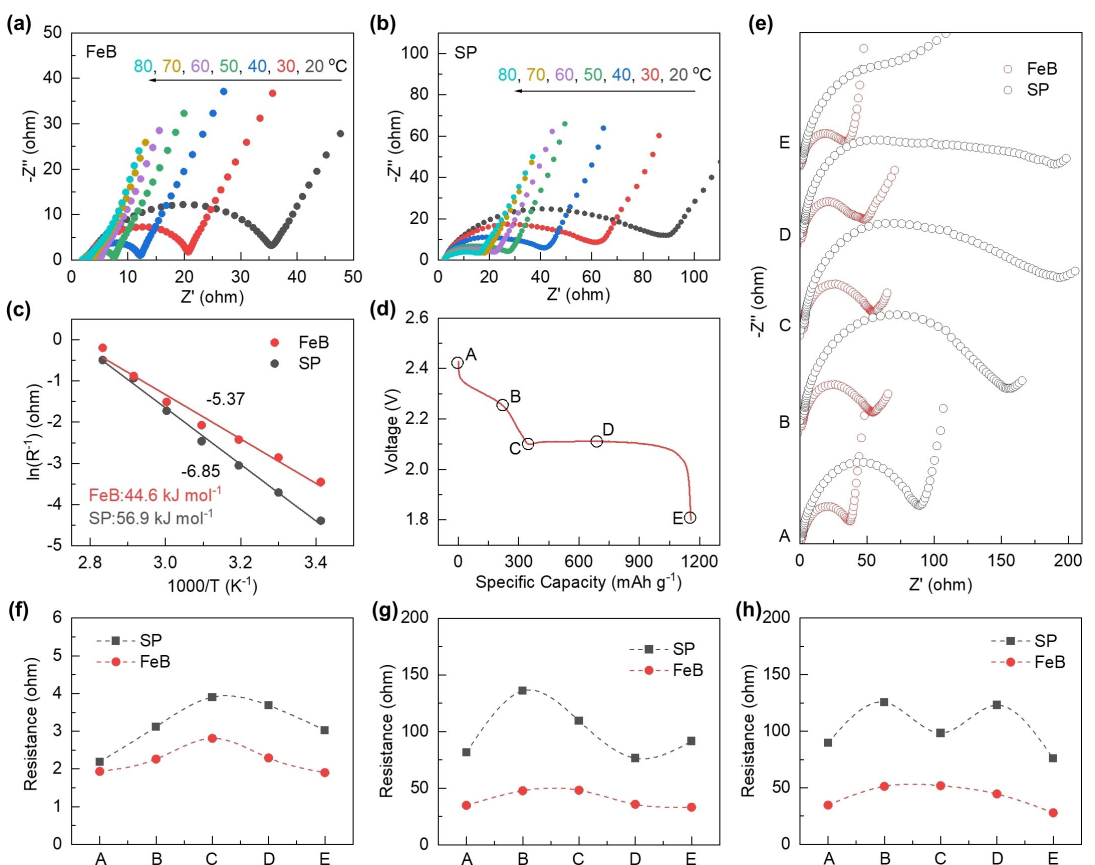


**Figure 6.** Nyquist plots of (a) FeB and (b) SP electrodes at different temperatures and (c) the corresponding active energies; (d) discharge profile, (e) Nyquist plots at different discharge states, and the evolution of (f)  $R_s$ , (g)  $R_{ct}$  and (h)  $R_w$  of different electrode during the discharge.

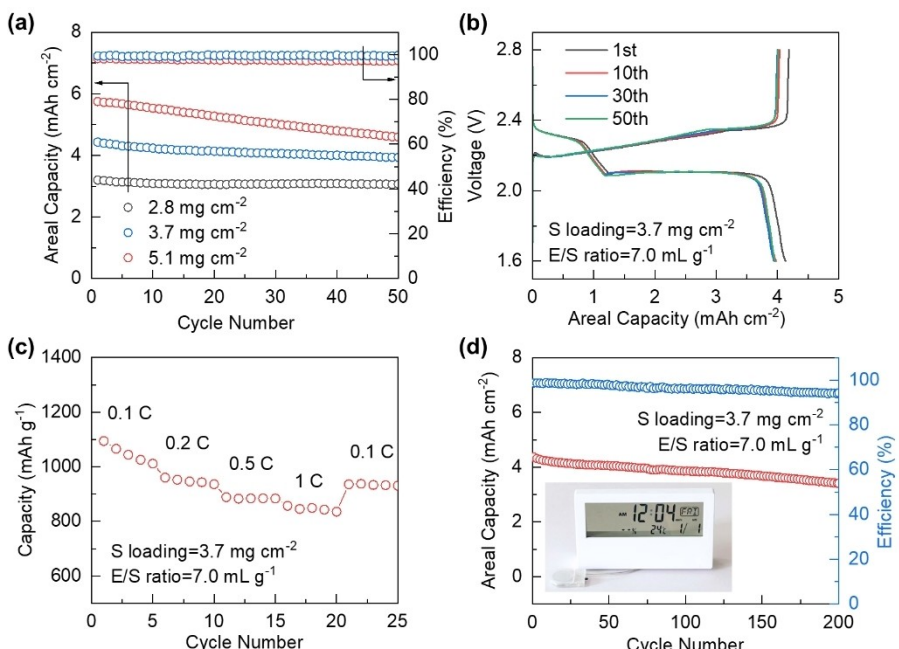


**Figure 7.** (a) Cycling performance of FeB electrodes under higher sulfur loadings; (b) voltage profiles at different cycles, (c) rate performance, and (d) long-term cycling performance of high-loading FeB electrodes.

of  $7.0 \text{ mAh g}^{-1}$  were recorded (Figure 7b). A clear two-plateau discharge profile can be still obtained and well maintained during cycling, suggesting excellent reaction reversibility and kinetics. Additionally, the rate performance of the high-loading FeB cell was also evaluated (Figure 7c). A decently high capacity of  $857.1 \text{ mAh g}^{-1}$  is still achievable at  $1 \text{ C}$ , confirming the favorable catalytic effect of FeB even under high-loading configurations. Furthermore, prolonged galvanostatic cycling was carried out as recorded in Figure 7d. The FeB electrode displays stable cycling with a high areal capacity of  $3.41 \text{ mAh cm}^{-2}$  retained after 200 cycles at  $0.1 \text{ C}$ , manifesting good reaction efficiency and reversibility under high-loading and limited-electrolyte conditions. Beyond that, the FeB cell successfully powers an electronic clock as shown in the inset of Figure 7d, demonstrating the good potential of the as-developed FeB electrocatalyst for practical application.

## Conclusions

In summary, we have developed a unique FeB as an advanced sulfur electrocatalyst for Li–S batteries. The well-designed molten-salt method effectively tames the SHS reactions, contributing to an ultrafine powdery FeB nanostructure. Combined with its metallic nature, the as-developed FeB not only facilitates rapid charge transfer but also affords efficient exposure of active interfaces, facilitating favorable host-guest interactions with LiPS. Moreover, the strong sulfur affinity of FeB enhances effective LiPS adsorption and catalytic conversions, promoting fast-kinetic and long-lasting sulfur electrochemistry, as confirmed by a series of physicochemical and electrochemical characterizations. Resultingly, Li–S cells based on the FeB catalyst realized excellent cyclability over 500 cycles, rate capability up to  $7 \text{ C}$ , and decent high-loading performance, showcasing a good promise for the development of high-performance and practically viable Li–S batteries.

## Experimental

**Preparation of FeB.** FeB was prepared via a molten salt method using  $\text{FeSO}_4$  and  $\text{NaBH}_4$  as the iron and boron sources, respectively. All the chemicals were used as received without further purification. Typically,  $0.3 \text{ g}$   $\text{FeSO}_4$  and  $1.0 \text{ g}$   $\text{NaBH}_4$  were ground and then blended with the salt medium ( $\text{NaCl}$  and  $\text{KCl}$  in a mass ratio of 1:1), followed by further grinding to achieve a homogenous mixture. The mass ratio of  $\text{FeSO}_4$  to the salt medium was controlled at 1:10. After that, the mixture was transferred to the tube furnace for annealing at  $1000^\circ\text{C}$  under an argon atmosphere, with a ramping rate of  $10^\circ\text{C min}^{-1}$  and a dwell time of 2 h. After cooling to room temperature, the product was immersed in deionized water to remove  $\text{NaBH}_4$  residue and salts. The final FeB product was collected after vacuum drying for over 12 h.

**Material characterizations:** The phase and crystalline structure were characterized by X-ray diffraction (XRD, Bruker-AXS D8 Advances). Scanning electron microscopy (SEM, FEI Quanta 250F) and transmission electron microscopy (TEM, FEI Talos F200X G2) were used to study the morphology and microstructure. The chemical status was analyzed by X-ray photoelectron spectroscopy (XPS, Thermo

Scientific K-Alpha). The UV-vis spectra were recorded on a UV-3600 SHIMADZU spectrophotometer to evaluate the LiPS concentration in the supernate.

**Electrochemical characterizations.** Sulfur electrodes were prepared by the typical slurry-casting method. The slurry was prepared by homogeneously dispersing element sulfur, super P, FeB, and PVDF (in weight ratio of 5:3:1:1) in N-methyl-2-pyrrolidone (NMP) solvent, and then cast onto the carbon-coated aluminum foil followed by vacuum dried at  $60^\circ\text{C}$  for 12 h. The sulfur loading on the electrodes was controlled at  $1.0\text{--}1.5 \text{ mg cm}^{-2}$  for regular evaluations. For electrochemical evaluation, the coin cells were assembled using the as-prepared sulfur cathode, Li foil as the anode, and porous polypropylene membrane (Celgard 2400) as the separator in an Ar-filled glove box ( $\text{O}_2 < 0.1 \text{ ppm}$ ,  $\text{H}_2\text{O} < 0.1 \text{ ppm}$ ). The electrolyte contains 1 M lithium bis (trifluoromethane) sulfonimide (LiTFSI) in 1,2-dimethoxyethane (DME) and 1,3-dioxolane (DOL) (1:1 in volume ratio) solvents with 2 wt.% lithium nitrate as the additive. The electrolyte addition was controlled at an E/S ratio of  $15 \text{ mL g}^{-1}$  for regular evaluation. Higher sulfur loadings (2.8, 3.7, and  $5.1 \text{ mg cm}^{-2}$ ) and less electrolyte addition (E/S of  $7.0 \text{ mL g}^{-1}$ ) were also applied to explore the battery performance under high-loading configurations. Galvanostatic charge/discharge cycling was performed by LAND testers (CT3002 A, Land Electronics Co., Ltd, Wuhan, China). The current and capacity were calculated based on the mass of sulfur ( $1 \text{ C} = 1675 \text{ mA g}^{-1}$ ). The CV measurement was conducted by a CHI604E electrochemical workstation (CH Instrument, Shanghai, China) with a scanning rate of  $0.1 \text{ mV s}^{-1}$ , and the EIS spectra were recorded within the frequency range of 0.1 to 100k Hz under an amplitude of 5 mV.

**Polysulfide adsorption test.** The  $\text{Li}_2\text{S}_6$  solution (50 mM) was prepared by dissolving elemental sulfur and  $\text{Li}_2\text{S}$  in a molar ratio of 5:1 in tetrahydrofuran (THF) under vigorous stirring. After that, the same amount of absorbent, i.e., SP or FeB, was added to the  $\text{Li}_2\text{S}_6$  solution and let stand for 6 h to compare the color variation.

**Kinetic characterizations.** The symmetric cells were fabricated by using identical electrodes and the electrolyte containing 0.1 M  $\text{Li}_2\text{S}_6$ . The electrodes were prepared by loading the same amount (around  $1 \text{ mg cm}^{-2}$ ) of SP or FeB on carbon cloth. The obtained symmetric cells were subject to CV measurement under varied scanning rates from 10 to  $50 \text{ mV s}^{-1}$ , while their EIS spectra were also recorded as described above. Apart from that, the  $\text{Li}_2\text{S}$  precipitation profiles were collected in asymmetric cells with FeB or SP cathodes and Li anodes. The electrolyte containing 0.25 M  $\text{Li}_2\text{S}_8$  was employed for the test. The cells were first galvanostatically discharged to 2.06 V and then subjected to potentiostatic discharge at 2.05 V for  $\text{Li}_2\text{S}$  nucleation and precipitation until the current was below  $10^{-5} \text{ A}$ .

## Acknowledgements

The authors thank the support from the National Natural Science Foundation of China (22109072, 22379069), China Postdoctoral Science Foundation (2021M691586), Open Project Foundation of National & Local Joint Engineering Research Center for Mineral Salt Deep Utilization (SF202105), and Fundamental Research Funds for the Central Universities (30922010304).

## Conflict of Interests

The authors declare no conflict of interest.

## Data Availability Statement

The data that support the findings of this study are available from the corresponding author upon reasonable request.

**Keywords:** lithium-sulfur battery · iron boride · molten salt · electrocatalysis · reaction kinetics

- [1] P. G. Bruce, S. A. Freunberger, L. J. Hardwick, J. M. Tarascon, *Nat. Mater.* **2012**, *11*, 19–29.
- [2] Z. W. Seh, Y. M. Sun, Q. F. Zhang, Y. Cui, *Chem. Soc. Rev.* **2016**, *45*, 5605–5634.
- [3] H. J. Peng, J. Q. Huang, X. B. Cheng, Q. Zhang, *Adv. Energy Mater.* **2017**, *7*, 1700260.
- [4] J. Tan, X. Y. Li, J. F. Shen, *Batteries & Supercaps* **2023**, *6*, e202200457.
- [5] G. R. Li, S. Wang, Y. N. Zhang, M. Li, Z. W. Chen, J. Lu, *Adv. Mater.* **2018**, *30*, 1705590.
- [6] Y. Chen, T. Y. Wang, H. J. Tian, D. W. Su, Q. Zhang, G. X. Wang, *Adv. Mater.* **2021**, *33*, 2003666.
- [7] D. Zhang, R. Gu, Y. X. Yang, J. Q. Ge, J. T. Xu, Q. J. Xu, P. H. Shi, M. X. Liu, Z. P. Guo, Y. L. Min, *Angew. Chem. Int. Ed.* **2024**, *63*, e202315122.
- [8] R. Gu, D. Zhang, S. Zhu, J. T. Xu, K. Ding, Q. W. Gao, Q. J. Xu, P. H. Shi, H. X. Li, Y. L. Min, *Adv. Funct. Mater.* **2024**, 2310747.
- [9] S. Kaskel, J. Q. Huang, H. Sakaabe, *Batteries & Supercaps* **2022**, *5*, e202200467.
- [10] Q. J. Shao, S. D. Zhu, J. Chen, *Nano Res.* **2023**, *16*, 8097–8138.
- [11] X. L. Ji, K. T. Lee, L. F. Nazar, *Nat. Mater.* **2009**, *8*, 500–506.
- [12] G. Jiménez-Martín, J. Castillo, X. Judez, J. L. Gómez-Urbano, G. Moreno-Fernández, A. Santiago, A. S. de Buruaga, I. Garbayo, J. A. Coca-Clemente, A. Villaverde, M. Armand, C. M. Li, D. Carriazo, *Batteries & Supercaps* **2022**, *5*, e202200167.
- [13] H. Y. Li, B. Cai, Y. Z. Song, W. L. Cai, G. R. Li, *Chin. Chem. Lett.* **2023**, *34*, 107811.
- [14] X. Liu, J. Q. Huang, Q. Zhang, L. Q. Mai, *Adv. Mater.* **2017**, *29*, 1601759.
- [15] W. C. Yue, X. Li, J. Zhao, Y. B. Gao, N. Gao, B. Li, G. M. Xia, S. M. Zheng, B. Wang, *Batteries & Supercaps* **2022**, *5*, e202200020.
- [16] D. H. Liu, C. Zhang, G. M. Zhou, W. Lv, G. W. Ling, L. J. Zhi, Q. H. Yang, *Adv. Sci.* **2018**, *5*, 1700270.
- [17] B. Wang, L. Wang, B. Zhang, Z. Kong, S. Y. Zeng, M. W. Zhao, Y. T. Qian, L. Q. Xu, *Energy Storage Mater.* **2022**, *45*, 130–141.
- [18] G. R. Li, H. Y. Li, H. B. Zeng, *J. Inorg. Mater.* **2022**, *37*, 152–162.
- [19] J. M. Zhang, X. L. Yan, Z. H. Cheng, Y. M. Han, Y. Zhang, Y. T. Dong, *J. Colloid Interface Sci.* **2024**, *657*, 511–528.
- [20] E. Lee, B. P. T. Fokwa, *Acc. Chem. Res.* **2022**, *55*, 56–64.
- [21] S. Carencq, D. Portehault, C. Boissière, N. Mézailles, C. Sanchez, *Chem. Rev.* **2013**, *113*, 7981–8065.
- [22] C. C. Li, X. B. Liu, L. Zhu, R. Z. Huang, M. W. Zhao, L. Q. Xu, Y. T. Qian, *Chem. Mater.* **2018**, *30*, 6969–6977.
- [23] B. Wang, L. Wang, B. Zhang, S. Y. Zeng, F. Tian, J. M. Dou, Y. T. Qian, L. Q. Xu, *ACS Nano* **2022**, *16*, 4947–4960.
- [24] H. Y. Li, G. X. Chen, K. L. Zhang, L. B. Wang, G. R. Li, *Adv. Sci.* **2023**, *14*, 2303830.
- [25] X. X. Sun, S. K. Liu, W. W. Sun, C. M. Zheng, *Chin. Chem. Lett.* **2023**, *34*, 107501.
- [26] J. H. Li, Z. S. Xiong, Y. J. Wu, H. Li, X. Y. Liu, H. J. Peng, Y. Y. Zheng, Q. Zhang, Q. B. Liu, *J. Energy Chem.* **2022**, *73*, 513–532.
- [27] Y. N. Wei, Z. T. Liu, S. L. Ran, A. L. Xia, T. F. Yi, Y. X. Ji, *J. Mater. Res.* **2017**, *32*, 883–889.
- [28] A. G. Merzhanov, *J. Mater. Chem.* **2004**, *14*, 1779–1786.
- [29] C. I. VillaVelázquez-Mendoza, J. L. Rodríguez-Mendoza, V. Ibarra-Galván, R. P. Hodgkins, A. López-Valdivieso, L. L. Serrato-Palacios, A. L. Leal-Cruz, V. Ibarra-Junquera, *Int. J. Surf. Sci. Eng.* **2014**, *8*, 71–91.
- [30] C. Y. Fu, J. L. Fan, Y. R. Zhang, H. Y. Lv, D. K. Ji, W. J. Hao, *J. Colloid Interface Sci.* **2023**, *634*, 804–816.
- [31] O. V. Zhdanova, M. B. Lyakhova, Y. G. Pastushenkov, *Met. Sci. Heat Treat.* **2013**, *55*, 68–72.
- [32] Y. H. Liu, L. Meng, L. Zhang, *Thin Solid Films* **2005**, *479*, 83–88.
- [33] J. A. Glasscock, P. R. F. Barnes, I. C. Plumb, N. Savvides, *J. Phys. Chem. C* **2007**, *111*, 16477–16488.
- [34] Q. Bie, P. B. Li, H. Cheng, S. J. Zheng, J. Yu, L. Yu, F. Wang, R. Wu, J. D. Chen, J. S. Chen, *Batteries & Supercaps* **2022**, *5*, e202200196.
- [35] T. T. Xie, G. Q. Song, G. L. Wang, P. Z. Feng, H. Xu, K. L. Lv, Y. B. Zhu, *J. Electron. Mater.* **2022**, *51*, 3705–3713.
- [36] Y. Bai, C. Wu, F. Wu, L. X. Yang, B. R. Wu, *Electrochim. Commun.* **2009**, *11*, 145–148.
- [37] D. W. Zhu, J. T. Xu, K. Ding, Q. J. Xu, P. H. Shi, Y. L. Min, *Adv. Funct. Mater.* **2023**, *33*, 2213822.
- [38] Y. C. Zhang, P. Zhou, R. F. Huang, C. Y. Zhou, Y. Liu, H. Zhang, X. W. Huo, J. Zhao, Z. K. Xiong, B. Lai, *J. Hazard. Mater.* **2023**, *443*, 130386.
- [39] C. C. Qiang, L. Zhang, H. L. He, Y. Y. Liu, Y. Y. Zhao, T. Sheng, S. J. Liu, X. L. Wu, Z. Fang, *J. Colloid Interface Sci.* **2021**, *604*, 650–659.
- [40] Q. L. Zou, Y. C. Lu, *J. Phys. Chem. Lett.* **2016**, *7*, 1518–1525.
- [41] L. S. Fan, H. X. Wu, X. Wu, M. X. Wang, J. H. Cheng, N. Q. Zhang, Y. J. Feng, K. N. Sun, *Electrochim. Acta* **2019**, *295*, 444–451.
- [42] R. R. Li, H. J. Shen, E. Pervaiz, M. H. Yang, *Chem. Eng. J.* **2021**, *404*, 126462.
- [43] R. R. Li, H. Sun, C. Y. Chang, Y. Yao, X. Pu, W. J. Mai, *J. Energy Chem.* **2022**, *75*, 74–82.
- [44] G. R. Li, F. Lu, X. Y. Dou, X. Wang, D. Luo, H. Sun, A. P. Yu, Z. W. Chen, *J. Am. Chem. Soc.* **2020**, *142*, 3583–3592.
- [45] W. Xiao, K. Yoo, J. H. Kim, H. Y. Xu, *Adv. Sci.* **2023**, *10*, 2303916.
- [46] F. Y. Fan, W. C. Carter, Y. M. Chiang, *Adv. Mater.* **2015**, *27*, 5203–5209.
- [47] G. R. Li, W. L. Qiu, W. J. Gao, Y. J. Zhu, X. M. Zhang, H. Y. Li, Y. G. Zhang, X. Wang, Z. W. Chen, *Adv. Funct. Mater.* **2022**, *32*, 2202853.
- [48] N. Ding, J. Schnell, X. D. Li, X. S. Yin, Z. L. Liu, Y. Zong, *Chem. Eng. J.* **2021**, *412*, 128559.
- [49] Z. F. Deng, Z. A. Zhang, Y. Q. Lai, J. Liu, J. Li, Y. X. Liu, *J. Electrochem. Soc.* **2013**, *160*, A553–A558.
- [50] Y. H. Wei, B. Y. Wang, Y. Zhang, M. Zhang, Q. Wang, Y. Zhang, H. Wu, *Adv. Funct. Mater.* **2021**, *31*, 2006033.
- [51] H. Q. Ji, Z. K. Wang, Y. W. Sun, Y. Zhou, S. J. Li, J. Q. Zhou, T. Qian, C. L. Yan, *Adv. Mater.* **2023**, *35*, 2208590.

Manuscript received: February 28, 2024

Revised manuscript received: April 7, 2024

Accepted manuscript online: April 8, 2024

Version of record online: May 8, 2024